Title

Morphology and Transport of Multivalent Cation-Exchanged Ionomer Membranes Using Perfluorosulfonic Acid–Ce Z+ as a Model System

Journal

ACS Applied Polymer Materials, 2(8)

ISSN

2637-6105

Authors

Baker, Andrew M
Crothers, Andrew R
Chintam, Kavitha
et al.

Publication Date

2020-08-14

DOI

10.1021/acsapm.0c00633

Peer reviewed

Morphology and Transport of Multivalent Cation-Exchanged Ionomer Membranes using Perfluorosulfonic Acid-Ce^{z+} as a Model System

Andrew M. Baker[1], Andrew R. Crothers[2], Kavitha Chintam[1], Xiaoyan Luo[2], Adam Z. Weber[2], Rod L. Borup[1], Ahmet Kusoglu[2,*]

1. Los Alamos National Laboratory, Los Alamos, New Mexico 87545, USA
2. Lawrence Berkeley National Laboratory, Berkeley, California 94720, USA

Abstract

Perfluorosulfonic acids (PFSAs), are commonly used as solid polymer electrolyte membranes (PEMs) in electrochemical energy devices, where they are vulnerable to attack by hydroxyl radical species during operation, which reduces their effectiveness. A popular strategy to combat this problem is to introduce radical scavengers like cerium (Ce) ions that neutralize these species before they attack the PFSA. Such cation doping creates a multi-ion system, in which understanding the mechanisms of cation solvation and transport becomes important for effective design and utilization of PFSA-cation systems. Ce ions also provide a representative model system for multi-cation-exchanged ionomers in electrochemical systems. In this study, hydration and conductivity measurements, along with X-ray fluorescence and scattering, are employed to elucidate how Ce ion exchange alters PFSA's ionic solvation as well as nano- and mesoscale morphology which ultimately control its ion transport properties. A molecular transport model is used to delineate the impact of Ce ions on the local solvation structure of water in the membrane from mesoscale changes of the transport pathways. The combined experimental and theoretical analysis reveals a nonlinear decrease in conductivity driven by cation solvation at the molecular level and morphological changes at larger length scales. Migration-diffusion coupling, its nonlinear dependence on ion-exchange and hydration, and its overall implications for ionomer performance are also discussed in order to provide an applicable case study. These findings have the potential to be translated into other mixed cation-ionomer systems for a wide range of energy and environmental devices.

Keywords: Ionomers, structure-property relationships, cation doping, concentrated solution theory, ion transport

* Corresponding author = akusoglu@lbl.gov
a. Present address = Nikola Motor Company, Phoenix, Arizona 85040, USA
b. Present address = Northwestern University, Evanston, Illinois 60208, USA

1. Introduction

With the advent of many electrochemical energy storage and conversion devices, such as flow batteries, electrolyzers, and fuel cells, there is a need to understand ion transport phenomena in these materials. Such systems typically rely on ion-conducting polymers, known as ionomers, as separators and solid electrolytes. While protons are generally the species of interest, other cations of varying oxidation states are present as redox species (in flow batteries, chlor-alkali, electrolysis),[1] radical scavengers or de-alloyed metals from Pt (in fuel cells),[2,3] or contaminants, in general,[4,5] leading to complex poly(anion)-cation and cation-proton interactions, collectively impacting ion transport and device functionality.[6]

A widely used ionomer in these applications is perfluorosulfonic acid (PFSA), due to its remarkable ion transport properties within a mechanically robust matrix.[6] PFSA's hydrophobic fluorocarbon backbone and fixed hydrophilic sulfonate end groups (referred to as "sulfonate groups" throughout the text) that, upon hydration, forms a phase-segregated nanostructure that enables ion transport (*i.e.*, protons and cations).[6] While this material is commonly utilized and studied for polymer electrolyte fuel cells (PEFCs) and electrolyzers, it is also a representative system to understand the roles of electrolyte properties and structure-functionality on electrochemical device performance.

Despite its chemical stability under a wide range of conditions, the PFSA polymer is still vulnerable to attack by radical species such as HO•, HOO• and H•, which originate from the decomposition of hydrogen peroxide (H_2O_2), leading to PFSA degradation.[7–9] Radical attack causes scission of the polymer chains, leading to its irreversible "unzipping" and subsequent release of fluorinated degradation products into reactant outlet streams,[10] which is exacerbated during hot and dry operating conditions.[11,12] This attack leads to global thinning of the membrane during operation,[13] which can further enhance peroxide/radical generation due to increased reactant crossover.[14,15] Furthermore, chemical and mechanical degradation are interdependent: radical attack diminishes the mechanical properties of the ionomer, such as tensile strength, ductility, fracture toughness, and creep resistance, which can increase its susceptibility to physical failure under mechanical stress.[16–18] Mechanical stress can also reduce the activation energy necessary for chemical degradation processes to proceed.[19]

An effective strategy to mitigate membrane degradation is to employ scavengers that can neutralize radical species. Cerium cations (herein referred to as "Ce ions") or oxides (*e.g.*, ceria)

are commonly used in PEFC membrane electrode assemblies (MEAs) because of their ability to react with and neutralize radicals rapidly and reversibly, which drastically improves PFSA durability. Ce ions[7] or ceria/ceria-based nanomaterials[20–22] have been shown to reduce fluoride emissions and improve voltage stability during accelerated PEFC durability testing by 1-3 orders of magnitude. Owing to its facile redox chemistry and stability in acidic media, Ce^{3+} is oxidized by HO•, and Ce^{4+} is reduced by H_2O_2, which is readily available in the MEA under typical operating conditions.[8] Due to the relatively high concentration of H_2O_2 during PEFC operation and PFSA acidity, modeling suggests that > 99% of the Ce ions exist in the hydroxyl radical scavenging trivalent ion form.[23] These ionic species, though, can transport within the MEA due to gradients in ionic potential,[24–27] ion concentration,[27–30] and ionomer hydration.[31,32] Other factors, such as membrane compression[31,33] and degradation/detachment of cation-exchanged polymer fragments[31,34] could also cause undesired cation movement.

Ce ion transport has been quantified experimentally using *ex situ* techniques, at concentrations locally exceeding the initial value in both the polymer electrolyte membrane (PEM) and catalyst layer (CL) ionomer regions. In the plane of the active electrode area, Ce ions have been measured at relatively high concentrations near drier regions and at lower concentrations near wetter regions.[31,32] High concentrations of Ce have also been measured in the CLs using through-plane elemental analysis.[26,31,35] Modeling and experimental studies indicate that Ce ions initially situated in the PEM will migrate into the cathode CL ionomer, where they can saturate the sulfonic acid groups, depleting the PEM of Ce ions and displacing protons in the CL.[14,26,36] Furthermore, such saturation of CL ionomer may diminish performance,[37] especially during high current-density operation.[14,38] In this work, we move beyond these empirical observations to understand the genesis of cation transport in energy-conversion devices, in order to quantify it and its effects to ensure effective device design.

Although the literature is rich with studies on structure-property relationships of PFSA membranes fully exchanged with other cations,[24,39–46] there are few investigations on mixed cation-proton systems,[5,6,13,39,42] and a paucity of insights into the transport mechanisms of multivalent cations, such as Ce; those that exist are focused primarily on overall MEA performance and durability.[47–49] Thus, it is yet to be elucidated how the addition of Ce ions at controlled doping levels affects the membrane's structure and functionality. In this paper, we aim to delineate the roles of ion solvation and cation-proton interactions on the resulting variations to transport. While

Ce ions are commonly used additives in PEFCs, deconvoluting the intricate relationship between its local oxidation state and concentration, ionomer/ionic hydration state, and the resulting effects on both PFSA morphology and ion transport is not trivial. In this work, properties of PFSA membranes doped with Ce^{3+} and Ce^{4+}, such as water uptake, conductivity, and nano/mesoscale structural features, are measured, interrelated, and modeled to establish hydration-structure-transport relationships. The results are discussed to identify the key ion doping levels impacting ionomer functionality and cell performance and to elucidate the underlying transport mechanisms of cation complexes in solid-acid electrolyte systems. As a result, Ce ions in PFSA can be used as a model system to understand better these and other interrelated interactions governing ion transport from the nano- to mesoscales.

2. Experimental Methods

2.1 Membrane preparation

Nafion™ NR-211 PFSA membranes (Ion Power, Inc.) with nominal thicknesses of 25 μm were received in protonated (H^+) form. Membranes were cation-exchanged by soaking them in aqueous solutions of Ce(III) nitrate and Ce(IV) sulfate (Sigma Aldrich), to introduce a range of ion exchange fractions of cations of the corresponding charge. Ce^{3+} contents were controlled by adjusting the concentration of the external solution, while a range of Ce^{4+} exchange fractions were obtained by soaking specimens in saturated Ce(IV) sulfate solutions for different durations due to its low solubility. Afterward, the membranes were rinsed in deionized (DI) water to remove excess solution on the surface and subsequently dried at 25°C and 10% RH. Ce concentrations (C_{Ce}) in the membranes were measured using X-ray fluorescence (XRF). A QUANT'X energy dispersive XRF spectrometer (Thermo Fisher Scientific) with a 3.5 mm aperture, an aluminum filter, an accelerating voltage of 12 kV, a tube current of 1.98 mA, and a scan duration of 1 minute/point was used for all XRF measurements. The CeLα fluorescence peak (4.84 keV) and background were fit using integrated software, which was verified to obtain a peak intensity accuracy of > 99%. Ce fluorescence intensities were calibrated using 3 thin film standards (Micromatter) with a precision of ±5%, which yielded a linear calibration curve with $R^2 > 0.99$.

The saturated concentration of Ce^{Z+} in a dry PFSA ($C_{Ce(z),sat}$) is reached when every sulfonic acid group is bound to a Ce cation of charge, z_{Ce} (equal to +3 or +4):

$$C_{Ce,sat} = \frac{M_{Ce}\,\rho_{PFSA}}{z_{Ce}\,EW_{PFSA}} \quad (1)$$

where M_{Ce} is the atomic mass of Ce (140.11 g/mol), ρ_{PFSA} is the density of dry PFSA (1.97 g/cm^3), and EW_{PFSA} is the equivalent weight of the proton-form PFSA (nominally 1100 g/mol$_{SO3-}$). The latter two values were taken from the manufacturer spec sheet. We note that, while various treatments exist in the literature for calculation of EW in the presence of cations,[50] in this work, EW is defined based on the fraction of sulfonate groups in the membrane and, therefore, assumed to not change with Ce ion concentration.[a] For Ce^{3+} and Ce^{4+}, $C_{\mathrm{Ce},sat}$ was calculated to be 90.2 and 67.7 mg$_{Ce}$/cm$^3_{ionomer}$, respectively. Finally, using these values, the Ce ion exchange fraction (f_{Ce}) may be calculated as:

$$f_{\mathrm{Ce}} = \frac{C_{Ce}}{C_{Ce,sat}} \quad (2)$$

The calibration curves for Ce^{3+} and Ce^{4+} ion exchange are shown in **Figure S1a and b**, respectively. Ce-exchanged films were characterized in 3 locations, which yielded typical standard deviations of $f_{\mathrm{Ce}} < 0.05$.

2.2 Water uptake

Membrane water uptake was measured gravimetrically as a function of relative humidity (RH) using a dynamic vapor sorption (DVS) analyzer (Surface Measurement Systems) at 25°C. First, the samples were dried in the DVS at 0% RH and 25°C for 2 hours to set a standard "dry state" with an initial sample weight, M_0. The samples were then humidified from 0 to 90% RH with increasing RH steps of 10%, and then to 98% RH. Samples were dehydrated back to 0% RH with the same RH values and interval, but in the opposite sequence. Water (mass) uptake of the membrane, ΔM_W, was continuously determined from the weight change with respect to the initial "dry state" weight, M_0. At each RH step, the samples were equilibrated until the change in the sample weight, $\Delta M_W/M_0$, was less than 0.005%/min. The water content, λ, typically defined as the number of water molecules per sulfonate group, was calculated based on the measured water uptake, $\Delta M_W/M_0$:

[a] Assuming that in full Ce^{3+} exchange, the EW in proton from (1100 g/mol) increases by M_{Ce}/z_{Ce} (= 46 g/mol), and changes by < 4%, which results in a change in the calculated water content by λ = 0.4 for high hydration levels (λ > 10). This corresponds to less than 3% change for most doping levels in this study (< 80%).

$$\lambda = \frac{mol\ H_2O}{mol\ SO_3^-} = \frac{\Delta M_W / MW_{H2O}}{M_0 / EW_{PFSA}} + \lambda_{\text{res}} \quad (3)$$

where MW_{H2O} is the molecular weight of water (18.0 g/mol). The residual water content in the membrane that is present at 0% RH at 25°C (λ_{res}) was also measured from the weight loss after heating the samples at 120°C ($M_0 - M_{120C}$), until a stable weight was reached in the DVS chamber, given by the formula:[46,51]

$$\lambda_{\text{res}} = \frac{(M_0 - M_{120C}) / MW_{H2O}}{M_0 / EW_{PFSA}} \quad (4)$$

We also adopted a modified version of Equation (3) for Ce-doped PFSA to account for the cation solvation effects, which will be discussed in more detail in the Results section.

2.3 Conductivity

In this study, both the in-plane and through-plane conductivities of the specimens were measured. The through-plane conductivity was measured as a function of RH and temperature with a MTS 740 Membrane Test System (Scribner Associates, Inc.) and the in-plane conductivity was measured using a four-electrode BT-110 conductivity cell (Scribner Associates, Inc.). For the through-plane conductivity tests, AC impedance measurements were performed under controlled humidity and temperature with an SI 1260 impedance/gain-phase analyzer (Schlumberger Technologies, Inc.) and ZPlot software (Scribner Associates, Inc.). Membranes with dimensions of 10 mm × 30 mm were sandwiched between SGL 10BC gas-diffusion layers (GDLs). The GDLs were attached to the platinum source electrode with conductive carbon paint. The assembly was compressed with a load of approximately 2.15 ± 0.02 MPa measured by a calibrated force spring and dial displacement indicator. In accordance with standard procedures,[52] samples were first kept at 30°C and 70% RH under a nitrogen atmosphere for 2 hours at the beginning of the test. Afterward, samples were dried to 20% RH with a step of 10% RH, and then hydrated to 90% with increment intervals of 10% RH, then to 95 and 98% RH, similar to the protocol used for the water-uptake measurements described above. Samples were preconditioned for 30 min at each step and then the membrane resistance was measured using voltage-controlled frequency-sweep spectroscopy (10 mVAC at 0 VDC, 10 MHz to 1 Hz, 10 steps/decade). The conductivity (κ) was calculated as:

$$\kappa = \frac{L}{RA} \quad (5)$$

where, for through-plane measurements, L is the thickness of the membrane taken as the average of measurements before and after the tests, R is the resistance derived from the intercept of the high-frequency impedance with the real axis, and A is the overlapping area of the platinum source electrodes (0.5 cm^2).

For in-plane conductivity measurements, two setups were employed for high- and low-temperature testing. In the first setup, membranes were cut into 14.6 mm wide strips and placed in the four-probe BT-110 conductivity cell. Prior to measurement, samples were equilibrated in H_2 at 80°C and 80% RH using a fuel-cell test stand (Fuel Cell Technologies) for 1 hour to ensure consistent thermal and hydration history. Specimens were then equilibrated at either 50 or 80°C in 80% RH H_2 for 15 minutes, and tested sequentially at 30, 50, 80, and 100% RH, with 15 minute equilibrations each. 30°C measurements were also performed at 100% RH, using an identical equilibration procedure. Conductivity of membranes in contact with liquid water (denoted throughout the text as "liquid-equilibrated") were performed by immersing samples in 18 MΩ DI water maintained at 30, 50, or 80°C. A DC potential sweep was applied using a BioLogic SP-50 potentiostat from -0.1 to 0.1 V at 10 mV/s. In addition, a membrane testing system (MTS 740, Scribner Associates Inc.) equipped with a Solartron 1286 DC potentiostat and a BT-110 conductivity cell was used for low-temperature testing under the same conditions as the through-plane measurements. From these measurements, the in-plane conductivity was calculated using Equation (5), where $\frac{1}{R}$ is the slope of the voltammogram, L is the distance between the voltage reference and sense electrodes (4.25 mm), and A is the cross-sectional area of the membrane.

2.4 Small- and wide-angle X-ray scattering

Small/wide-angle X-ray scattering (SAXS/WAXS) experiments were performed in beamline 7.3.3 of the Advanced Light Source (ALS) at Lawrence Berkeley National Laboratory (LBNL). The X-ray wavelength was 0.124 nm, with a monochromator energy resolution of E/dE of 100, and the presented patterns were collected using a 2-D Dectris Pilatus 2 M CCD detector (0.172 mm x 0.172 mm pixel size). The scattering wave vector, $q = 4\pi \sin(\theta/2)/\lambda$, where θ is the scattering angle, was in the range of 0.001 to 0.04 $Å^{-1}$ for SAXS and 0.5 to 3 $Å^{-1}$ for WAXS. *In situ* liquid-equilibrated scattering experiments were conducted by immersing the samples in 25°C

liquid water using custom-designed sample holders with X-ray transparent Kapton windows, as described previously.[46,53] The collected 2-D scattering patterns were azimuthally integrated to generate 1-D intensity profiles, I(q), which were corrected by subtracting the background scattering. From the SAXS data, hydrophilic domain spacing and full-width half-max (FWHM) were calculated using a Gaussian fit to the ionomer scattering peak. The relative degree of crystallinity was calculated from the ratio of the integrated area of the crystalline and amorphous peaks (See the Supporting Information [SI] for details).

3. Results

Before proceeding with the results, it is instructive to explain how the quantity of cations in the ionomer membrane system (Ce ions + the remaining protons) changes as a function of Ce ion doping level, f_{Ce} . As the membrane is de-protonated by increasing f_{Ce}, multivalent Ce ions of charge z_{Ce} replace z_{Ce} protons in order to satisfy electroneutrality, resulting in a decrease in the *total* number of cations in the system. Here, we define the cation mole fraction (f_{cation}) as the ratio of total cations in the membrane to the number of sulfonate groups, as shown in **Figure 1a**, which is represented as:

$$f_{\mathrm{cation}} = f_{\mathrm{proton}} + \frac{1}{z_{Ce}} f_{\mathrm{Ce}} = (1 - f_{\mathrm{Ce}}) + \frac{f_{\mathrm{Ce}}}{z_{Ce}} \tag{6}$$

Which becomes 1 in proton form ($f_{\mathrm{Ce}} = 0$), and decreases linearly to 1/3 or 1/4 in the fully-exchanged Ce^{3+} or Ce^{4+} forms, respectively, ($f_{\mathrm{Ce}} = 1$), as shown in **Figure S2.**

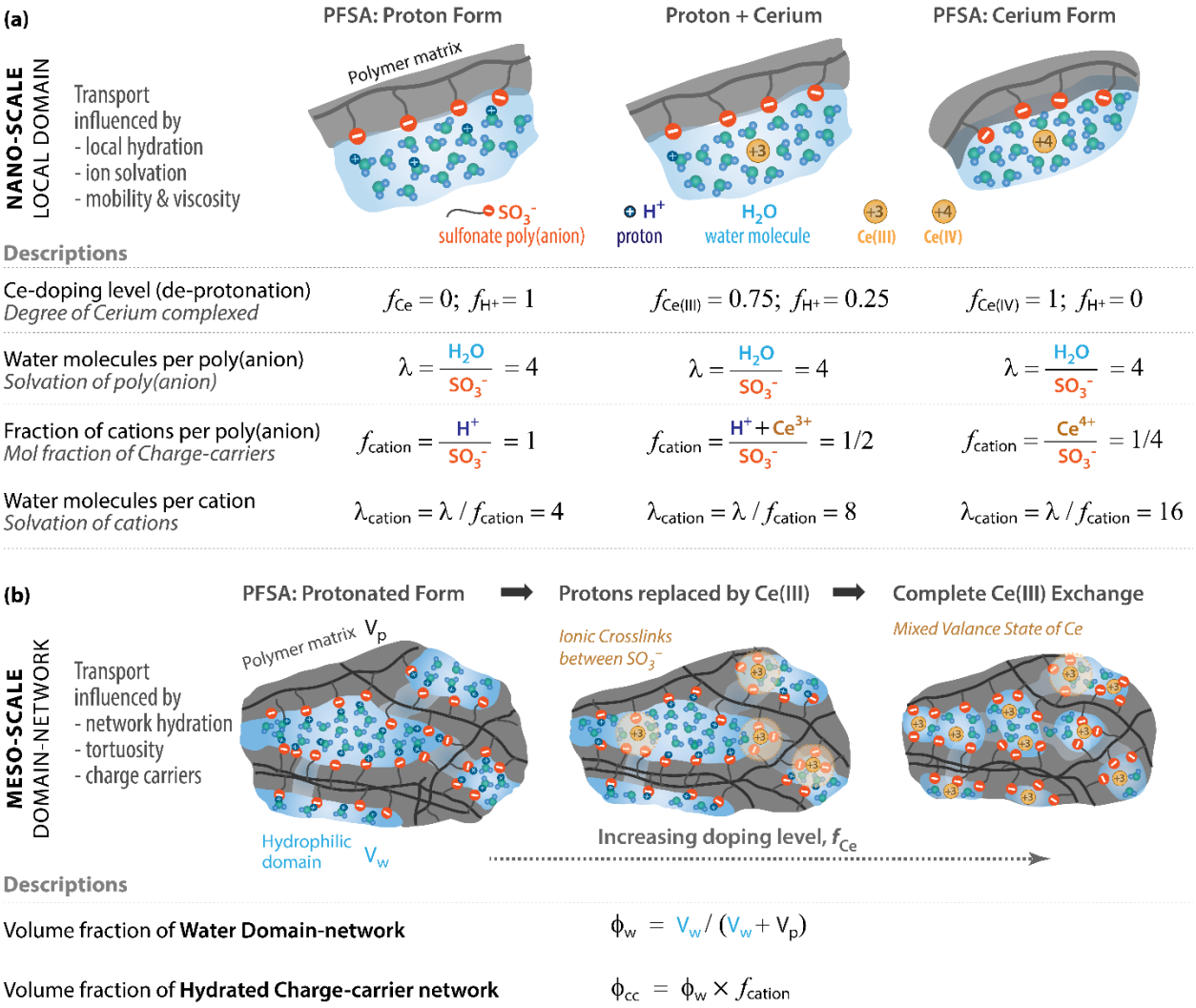

Figure 1 – Illustration of proposed changes in the PFSA structure at the **(a)** nano- and **(b)** mesoscales as a function of Ce ion doping level (f_{Ce}). In **(a)**, water content and cation fraction calculated in Equations (6)-(9) are shown for a representative ionomer chain containing four sulfonate groups neutralized with various counter-ions (*i.e.*, protons and/or Ce ions). The descriptions are included to highlight the significant changes in numerical values of ionomer hydration depending on if the fraction of cation-water complexes is included.

3.1 Water Uptake and Hydration Behavior

Inspection of the water-sorption isotherms in **Figure 2a** reveals that with increasing f_{Ce}, λ increases at lower RH (0 to 10%), but decreases at higher RH levels, with 98% RH showing the most dramatic reduction in hydration. λ increases from f_{Ce} = 0 to f_{Ce} = 0.5 at 0% RH and remains almost constant at 10% RH. Noting that λ at 0% RH represents the residual water in the membrane, exchanging protons with Ce ions slightly enhances the membrane's bulk water retention capacity at this RH. As shown in **Figure 2b**, membranes exchanged with Ce ions uptake less water molecules per sulfonate group for f_{Ce} > 0.5, with a > 20% decrease at high f_{Ce} and RH levels. For f_{Ce} < 0.5, the impact of Ce^{3+} or Ce^{4+} on weight uptake and water content is negligible. To account for the changing fraction of total protons and Ce ions in the system and glean insights into their solvation at different length scales, modified descriptions for hydration at nano- and mesoscales are proposed. These definitions are illustrated and explained in greater detail in **Figure 1a.**

First, in accordance with Shi et al.,[46] the definition of nanoscale hydration (λ_{cation}), is adopted, which represents the number water molecules locally associated with the cations in the system (f_{cation}) and is a measure of solvation of the remaining cations:

$$\lambda_{cation} = \frac{mol\ H_2O}{mol\ H^+ + mol\ Ce^{z+}} = \frac{mol\ H_2O}{mol\ SO_3^-} \times \frac{mol\ SO_3^-}{mol\ H^+ + mol\ Ce^{z+}} \tag{7}$$

The equation above can be combined with definitions of λ [Equation (3)] and f_{cation} [Equation (6)] and rewritten as:

$$\lambda_{cation} = \frac{\lambda(f_{Ce}, RH)}{f_{\mathrm{cation}}} = \frac{\lambda(f_{Ce}, RH)}{\left(1 - f_{\mathrm{Ce}} + \frac{f_{\mathrm{Ce}}}{z_{Ce}}\right)} \tag{8}$$

This expression establishes a relationship between the hydration of the sulfonate groups and the solvation of all cations in the system. It should also be noted that the λs used in Equation (8) are functions of both f_{Ce} and RH. This local hydration effect is isolated by normalizing λ_{cation} to their respective proton-form values at each RH (λ_{H+}), which converges to an exponentially-increasing function of f_{Ce} as shown in **Figure 2c**. Thus, λ_{cation} increases with increasing Ce ion doping, which indicates a higher fraction of water molecules interacting with cations.

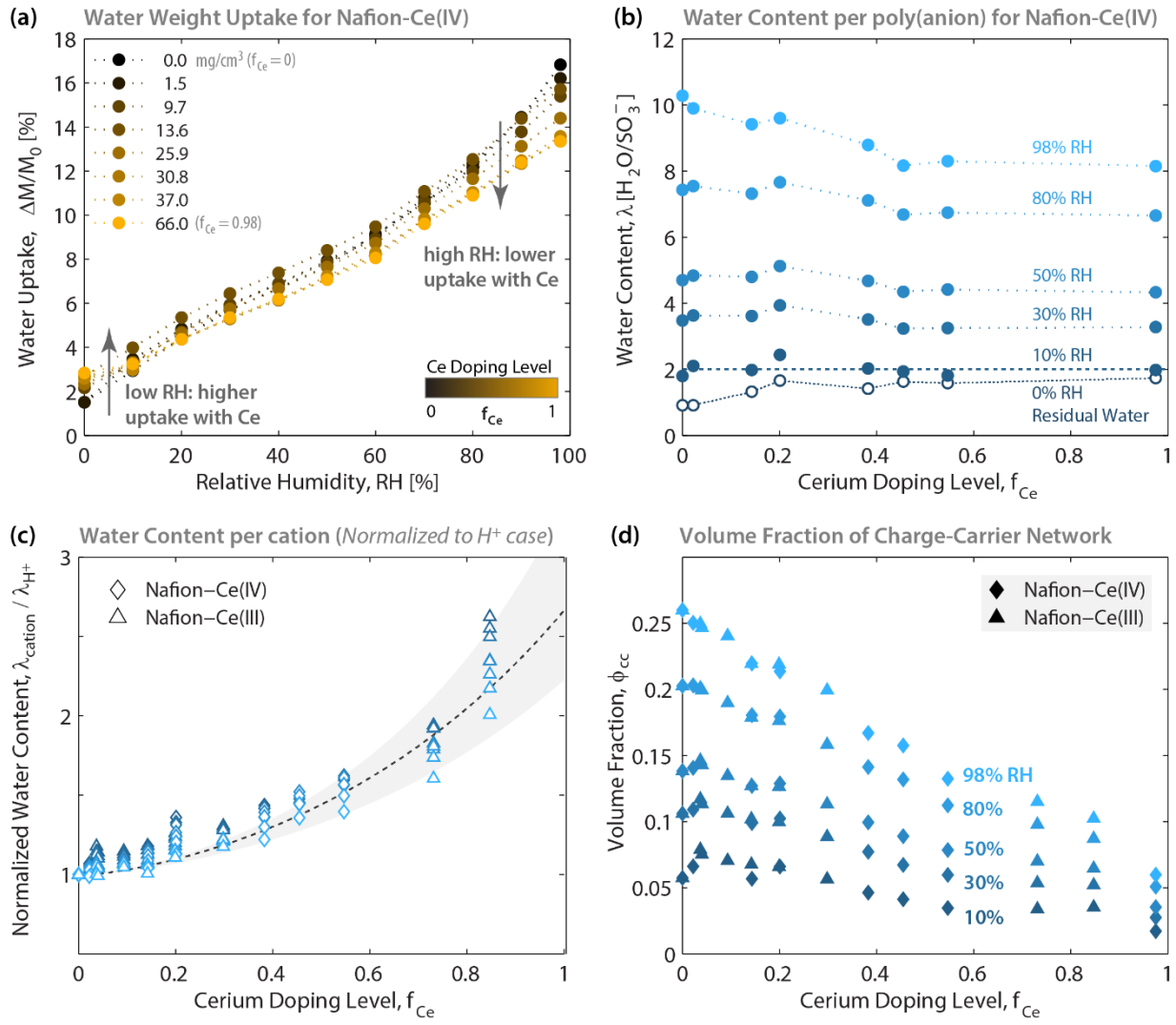

Figure 2 – **Hydration behavior of PFSA membranes exchanged with various amounts of Ce ions: (a)** Sorption isotherms for PFSA-Ce^{4+} at 25°C plotted in terms of weight change vs. relative humidity and **(b)** water molecules per sulfonate group (λ) vs. Ce^{4+} ion doping level at selected RH values. Effect of Ce doping on **(c)** water content per cation (λ_{cation}) normalized with respect to its initial value for proton form membrane (λ_{H+}), and **(d)** hydrated charge carrier network volume fraction (ϕ_{cc}). The lines in **(a)-(c)** are guides-for-the-eye. The values in **(b)-(d)** are shown at selected RH levels, where the same symbol colors are used for each RH. In **(c)** and **(d)** both Ce^{3+} (triangle symbols) and Ce^{4+} (diamond symbols) are used.

When hydration is characterized in terms of λ_{cation}, the effect of Ce ion doping presents a striking contrast: while increasing f_{Ce} slightly reduces the average λ, it greatly increases the number of water molecules per cation, λ_{cation}. This indicates that, despite a decrease in λ (water associated with fixed sulfonate groups) with increasing f_{Ce}, the remaining water molecules form

a higher degree of association with each Ce ion, resulting in increased values of λ_{cation} (water per mobile cation). This effect arises from electroneutrality and changes in the mole fraction of cations, as illustrated in **Figure 1a**. We attribute this effect to the high hydration number of Ce compared to protons (*i.e.*, large solvation energy; 9 H_2O in solution compared to proton's solvation by 3.6 to 4 H_2O,[2,54]), which is supported by molecular-dynamics simulations of multivalent cations in PFSAs which suggest strong solvation,[55] especially at low water contents.[56] This effect is seen more clearly in terms of water molecules per cation, a better measure of ion solvation, which increases by two-fold even at low RH, when the membrane is fully exchanged with Ce **(Figure 2c**).

To reconcile the discrepancy between the local, nanoscale hydration (λ_{cation}) and the macroscopically observed decrease in bulk water uptake (λ), another description for hydration is proposed based on the solvation of the varying amount of cations (f_{cation}) within the mesoscale ion-conducting hydrophilic domain network. ϕ_{w} is the volume fraction of this network, defined as:

$$\phi_{\mathrm{w}} = \frac{\lambda}{\lambda + \bar{V}_{\mathrm{p}}/\bar{V}_{\mathrm{w}}} \tag{9}$$

where $\bar{V}_{\mathrm{p}}$ and $\bar{V}_{\mathrm{w}}$ are the molar volumes of dry PFSA and water, respectively. $\bar{V}_{\mathrm{p}}$ can be estimated from the PFSA's EW and density: $\bar{V}_{\mathrm{p}} = EW_{PFSA}/\rho_{PFSA}$ and $\bar{V}_{\mathrm{w}}$ is 18.1 cm^3/mol.

Since all ions are assumed to be located within these hydrophilic domains,[57] the product of ϕ_{w} and f_{cation} quantifies the volume fraction of the *total* amount of charge carriers (*i.e.*, water and cations) in the hydrophilic domain network of PFSA (**Figure 1**). We define the "***hydrated charge carrier network***" volume fraction as:

$$\phi_{cc} = \phi_{\mathrm{w}} f_{\mathrm{cation}} \tag{10}$$

As shown in **Figure 2d**, the quantity ϕ_{cc} decreases continuously with increasing f_{Ce} due to exclusion of water with increased exchanged Ce ions. This suggests reduced concentrations of hydrated charge carriers at the mesoscale, despite greater cation solvation at the nanoscale (**Figure 2c**). These trends imply that in cation-exchanged systems, characterization and quantification of hydration changes distinctly across these length scales (**Figure 1**) and strongly depends on both the solvation and concentration of the multivalent ions.

3.2 Conductivity

3.2.1 Effect of Temperature in Liquid Water

The effect of temperature on the conductivity of Ce ion-exchanged PFSA equilibrated in liquid water can be seen in **Figure 3**. Conductivity decreases monotonically as f_{Ce} increases (**Figure 3a**). Furthermore, when the values are normalized to the conductivity of proton-form PFSA at each temperature (κ_{H^+}, which occurs at f_{Ce} = 0), all values overlap on a single curve (**Figure 3a, inset**). This behavior implies that, when equilibrated in liquid water, the conductivity of Ce-doped PFSAs can be expressed mathematically as a combination of a f_{Ce}-dependent, thermally-activated resistance (R_T) and a hydration-driven resistance (R_H):

$$R_{H+/Ce} = R_T(T, f_{Ce}) \times R_H(f_{Ce}) \quad (11)$$

For the latter term, this decrease in conductivity can be described by a rule-of-mixtures between PFSA in proton-form (κ_{H+}) and fully ion-exchanged form (κ_{Ce}, which occurs at f_{Ce} = 1). This behavior implies a smooth transition of properties that result in reduced conductivity in the κ_{Ce} case, which will be explored in the following sections.

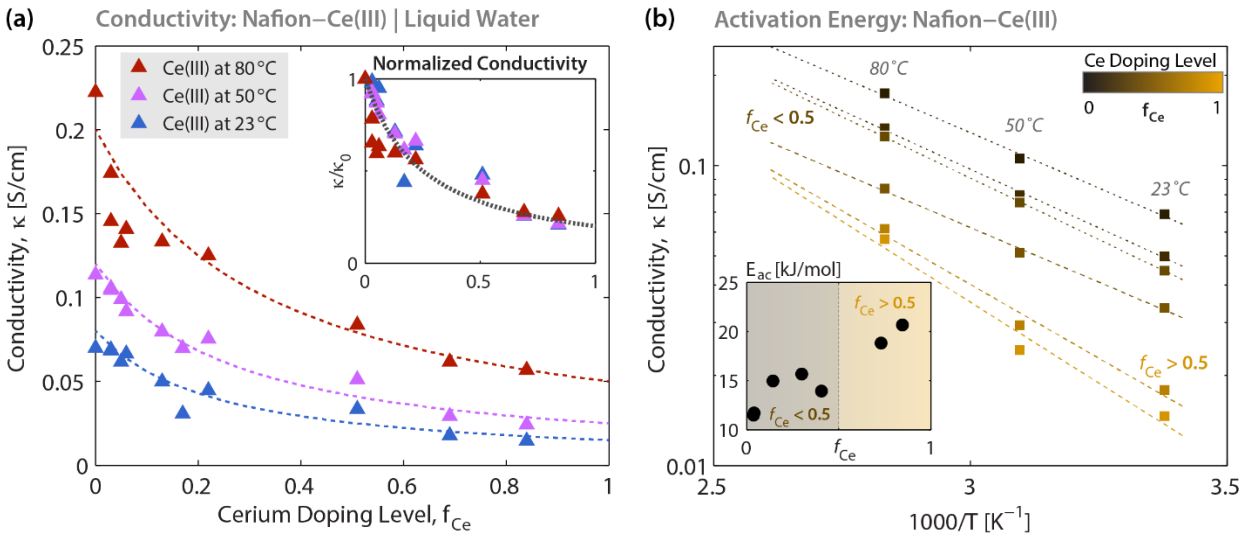

Figure 3 – **(a)** Conductivity of PFSA-Ce^{3+} at different temperatures equilibrated in liquid water as a function of the Ce ion doping level (f_{Ce}). **(b)** Arrhenius plot of conductivity vs. temperature of PFSA-Ce^{3+} samples equilibrated in liquid water. Dotted lines in **(a)** are a guide-for-the-eye representing rule-of-mixtures between κ_{H+} and κ_{Ce}.

While this approximation can capture the experimental data (lines in **Figure 3a**), the effect of temperature on conductivity summarized in an Arrhenius plot in **Figure 3b** shows a thermally-

activated contribution to resistance [R_T in Equation (11)]. As shown in the inset of **Figure 3b**, the activation energy for conductivity of liquid-equilibrated samples also increases at higher f_{Ce}, from 12 kJ/mol at f_{Ce} < 0.5 to over 20 kJ/mol after f_{Ce} > 0.5.

3.2.2 Effects of Temperature and Humidity in Vapor

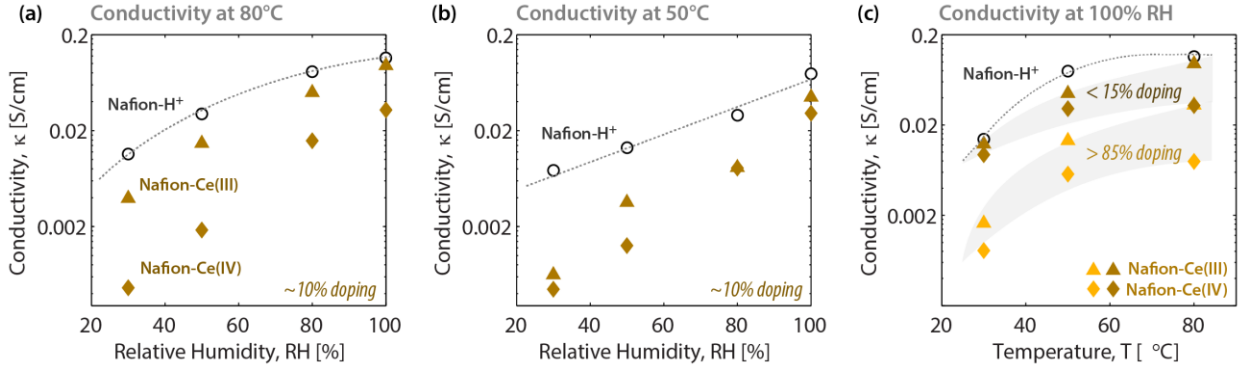

Figure 4 – Effects of relative humidity on the conductivity of PFSA-Ce^{Z+} membranes exchanged with low doping levels of Ce^{3+} and Ce^{4+} (f_{Ce} = 0.14 and 0.093, respectively), at **(a)** 80°C and **(b)** 50°C. **(c)** Conductivity of PFSA-Ce^{Z+} membranes at 100% RH shown as a function of temperature for low and high doping levels of Ce (f_{Ce} < 0.15 and > 0.85, respectively).

Conductivity measurements were carried out in water vapor to examine the effects of temperature and RH on the charge transport of Ce-exchanged and proton-form membranes (**Figure 4**). Membranes doped with ~10% Ce^{3+} and Ce^{4+} exhibit lower conductivity at all temperature and humidity values investigated. Conductivity in vapor also has a positive correlation with temperature, as was the case with conductivity in liquid water (**Figure 3**). Nevertheless, the relative decrease in κ compared to the H^+ form membrane is higher at higher temperatures and lower RHs (*i.e.*, hot and dry conditions). Thus, the presence of Ce ions in the membrane causes the most detrimental effects on transport in this T/RH regime, which has key implications for membrane performance – as these are relevant during device operation.[32,58] For example, in PEM fuel cells, Ce ions tend to accumulate near drier regions in the plane of the active electrode area,[31,32] thereby locally exacerbating its impact on transport resistance. While such a reduction in membrane conductivity is apparent for f_{Ce} < 0.15, the effects are exacerbated at f_{Ce} > 0.85, resulting in an order-of-magnitude lower conductivity (**Figure 4c**). Lastly, Ce^{4+} exhibits lower conductivity for each case relative to Ce^{3+}, and again, the effects are most pronounced under hot and dry conditions. Identical trends were observed across all other temperature and RH conditions tested (**Figure S3**).

3.3 Small- and wide-angle X-ray scattering

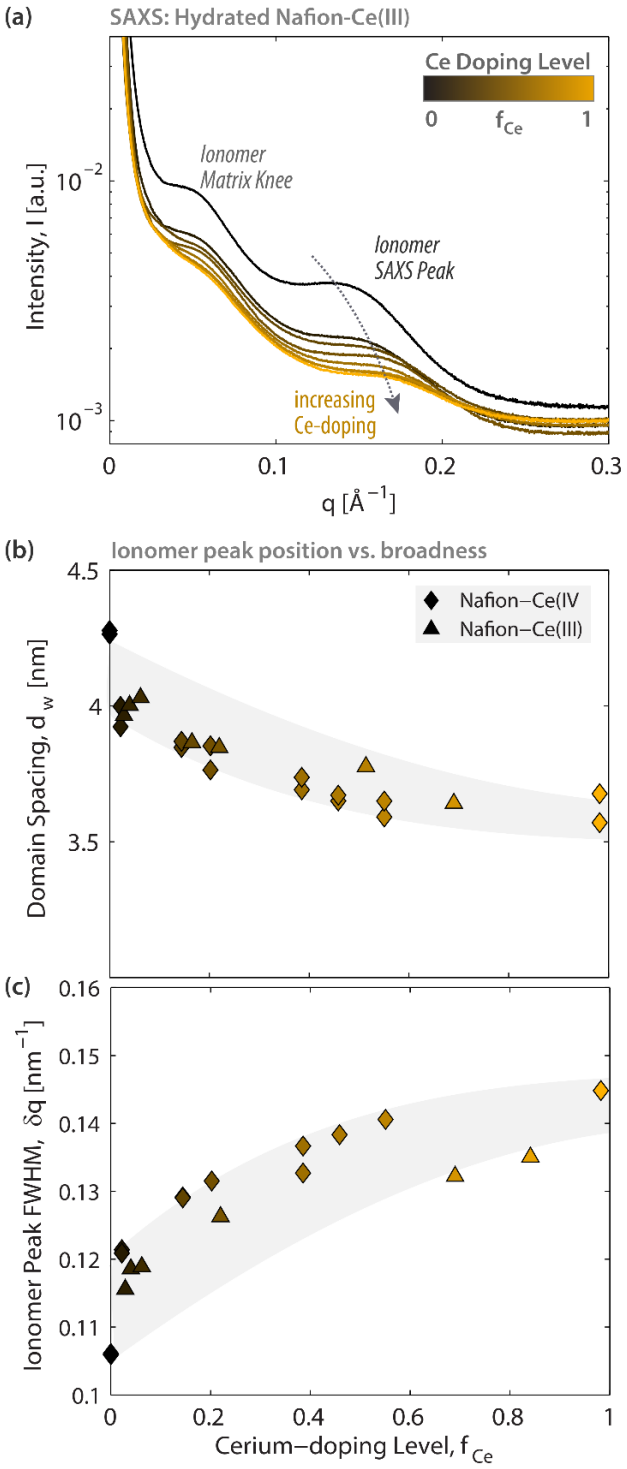

Figure 5 – Morphology changes in liquid-hydrated PFSA-Ce^{Z+} as a function of Ce ion doping level (f_{Ce}): **(a)** SAXS profiles for PFSA-Ce^{4+}, and **(b)** hydrophilic domain spacing and **(c)** ionomer peak full-width half-max (FWHM) for PFSA-Ce^{Z+}. Individual SAXS spectra, along with their corresponding fits are shown **Figure S4**. In **(b)** and **(c)** both Ce^{3+} (triangle symbols) and Ce^{4+} (diamond symbols) are used.

SAXS and WAXS were performed to investigate the morphological changes to PFSA as a function of f_{Ce}. From WAXS spectra, a continuous change in amorphous peak accompanied by a reduction in crystalline peak, especially above $f_{Ce} > 0.6$, is inferred (See **Figure S5a** in the SI for WAXS spectra and fitting procedures). This indicates a slight reduction to the relative degree of crystallinity which decreases from 15 to 13% with increasing f_{Ce} up to f_{Ce} = 0.5 (**Figure S5b**). The reduced crystallinity at higher doping levels could be related to the disruption of the crystallites formed by PFSA's fluorocarbon backbone chains, even though Ce ions primarily interact with the sulfonate groups in the hydrophilic regions of PFSAs.

To examine the impact of f_{Ce} on nano- and mesomorphology in the hydrated state, hydrophilic domain and network structures were analyzed from the SAXS profiles of liquid-equilibrated membranes exchanged with Ce ions. As shown in **Figure 5a**, even at low doping levels (f_{Ce} < 0.1), the ionomer peak of the SAXS spectra shifts strongly to higher q, indicating smaller hydrophilic domain spacing. Domain spacing decreases continuously with increasing f_{Ce}, although the values begin to reach a plateau after the 50% doping level, as observed in **Figure 5b**.

Another impact of Ce ion doping on nanomorphology is the broadening of the ionomer peak, which can be quantified by its FWHM (**Figure 5c**). The FWHM increases with increased f_{Ce}, indicating a weaker, more disordered degree of phase-separation between hydrophobic and hydrophilic domains.[6,59] As was the case with domain spacing and crystallinity, the FWHM curve flattens at f_{Ce} > 0.5. This result is analyzed with caution because the change in scattering signal could also arise from the electron density differences caused by the large Ce ions, especially at high doping levels.

Nevertheless, a critical Ce ion doping level of 50% (f_{Ce} = 0.5) is apparent, above which PFSA shows a lower degree of phase separation. The reduced connectivity of these domains is proposed to result in more tortuous pathways for ion and water transport**.** This observation is consistent with the effect of multivalent Ce ions bringing together multiple poly(anionic) sulfonate groups, per electroneutrality, which would create strong local ionic crosslinks within smaller, more clustered, domains as illustrated in **Figure 1b** and create farther distances between neighboring clusters. Such an effect would also lead to reduced mobility of chains near the ionic moieties. These two effects suggest a structural origin of reduced conductivity due to the introduction of multivalent cations, as discussed in more detail below.

4. Discussion and Transport Model

4.1 Conductivity-Hydration Correlation

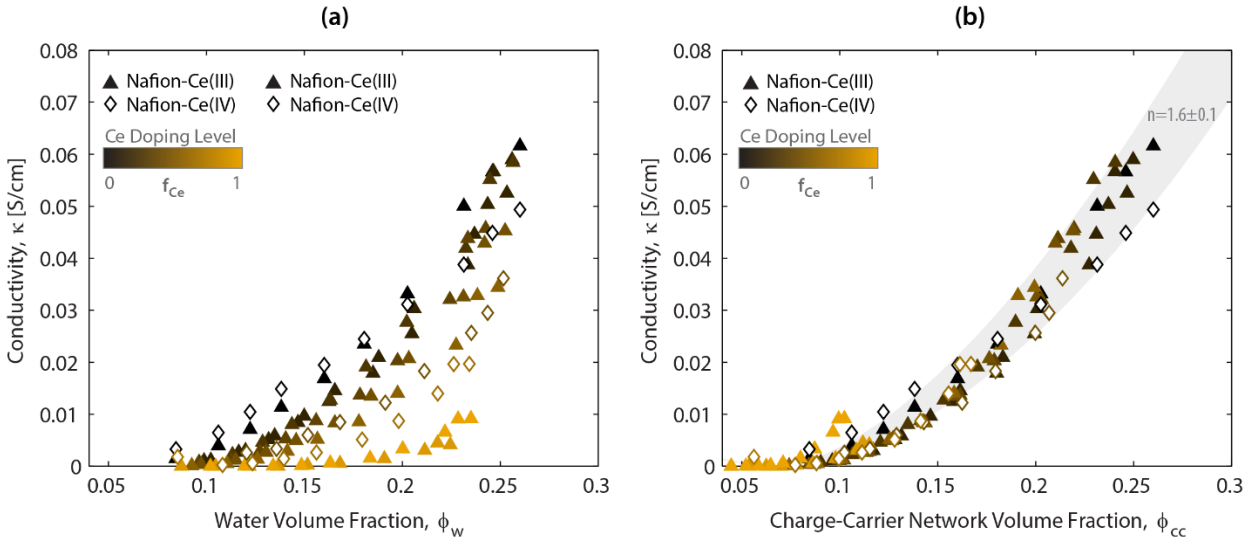

Figure 6 – Conductivity (κ) of PFSA-Ce^{Z+} membranes with various doping levels (f_{Ce}) of Ce^{3+} (closed symbols) and Ce^{4+} (open symbols) as a function of hydration plotted in terms of **(a)** water volume fraction (ϕ_w) and **(b)** hydrated charge carrier network volume fraction (ϕ_{cc}) described in **Figure 1**. The best fit for all measured data in **(b)** is shown with the curves enclosing the shaded area.

To isolate the effect of f_{Ce} on conductivity and hydration and search for a universal relationship between these parameters, their correlation is explored using the two representations of hydration, ϕ_w and ϕ_{cc}, shown in **Figure 1b**. A plot of κ vs. ϕ_w for various f_{Ce} shows a slightly nonlinear correlation, albeit with different slopes, which decreases monotonically as f_{Ce} increases (**Figure 6a**). The change in the slope of conductivity against hydration was previously reported for proton-form PFSAs, and associated with the ion exchange capacity and more recently modeled to be related to mesoscale network tortuosity.[6,60] Conductivity of an interconnected water domain-network as a function of the domain volume fraction is expressed as:

$$\kappa(\phi_w) = \kappa_0 \, (\phi_w - \phi_0)^n \tag{12}$$

where κ_0 is a temperature-dependent prefactor, and $\phi_0 = 0.05$ is the percolation threshold, which marks the minimum connectivity a membrane requires to facilitate ion transport.[6,56] The exponent, n, is a measure of hydrophilic domain network connectivity, and can be related to tortuosity; the lower the n, the more tortuous the transport pathways for ion conduction. **Figure 6a** shows that n

is a strong function of f_{Ce}, which implies increased tortuosity of the hydrophilic domain network as more Ce ions are added to the system, consistent with a less connected network structure proposed from the scattering results (**Figure 5c**).

As shown in **Figure 6b**, when plotted as a function of the hydrated charge carrier network volume fraction (ϕ_{cc}), conductivity converges for all f_{Ce} and z_{Ce}. This universal relationship suggests that it is not the fraction of water domains (*i.e.*, the *geometry* of interconnectivity), that affects the conductivity, alone, as seen in proton-form ionomers.[6] Instead, in this PFSA-Ce^{Z+} system, the volume fraction of the hydrated charge carrier network within the PFSA matrix (*i.e.*, the *chemical character* of interconnectivity) appears to most strongly underpin conductivity. This observation could have broad implications for the examination of transport properties in multivalent cation-exchanged ionomers: cation concentration and water volume fraction could be used together to model and analyze conductivity (and thus, cation transport properties[24,61]).

These different trends demonstrate the important roles of cation solvation and fraction, at both the nano- and mesoscales. While the nanoscale effect can be mathematically represented by water per cation (λ_{cation}), which increases with doping (**Figure 2c**), the mesoscale network effect is characterized by ϕ_{cc}, which decreases with doping (**Figure 2d**). In light of the above findings on structural and hydration changes due to doping, strong evidence is provided that suggests changes in transport properties could be linked to morphological changes in PFSA-Ce^{Z+} systems governed by ionic interactions and crosslinking. As f_{Ce} increases, it is proposed that ionic crosslinks by multivalent Ce ions disrupt the connectivity of the hydrophilic domain network, leading to smaller, more clustered water domains within a more amorphous polymer structure. This results in more tortuous ion conduction pathways and increased transport resistance of the hydrophilic domain network, which is consistent with the observed decrease in macroscopic conductivity. To better elucidate the origins of this phenomenon and the role of ion-water interactions in ion transport at multiple length scales, the changes in measured conductivity were analyzed using a transport model.

4.2 Modeling of Transport Mechanisms

Ce-exchanged membranes have significantly lower conductivity than proton-form membranes, which may be attributed to **(*i*)** the lower intrinsic mobility of Ce ions compared to protons;[62] **(*ii*)** the reduction of mobile water for protons to move through due to Ce ions strongly

binding water in its viscous solvation shell;[54] and ***(iii)*** interactions between Ce ions and multiple sulfonic acid moieties, which increase the heterogeneity of PFSA's hydrophilic transport network leading to increased tortuosity of proton and Ce ion transport pathways.

Using microscale theories for concentrated solution transport parameters, we recently showed that these effects on macroscopic conductivity could be delineated by expressing the conductivity as the combination of three distinct transport factors:[63]

$$\kappa = \kappa^{\infty}\left(\frac{\mu^{\infty}}{\mu}\right)\left(\frac{\phi_w}{\tau}\right) \tag{13}$$

The first term (κ^{∞}) is the *ideal conductivity* factor of a hydrophilic domain and is a function of water content and the infinite dilution diffusivities of protons and Ce ions. κ^{∞} accounts for **(*i*)** by quantifying the current carried by protons and Ce ions given their concentrations in the membrane and their mobilities. The second term ($\frac{\mu^{\infty}}{\mu}$) is the *viscosity factor* that incorporates **(*ii*)** by describing how solvation of Ce^{Z+} and H^{+} increases viscosity of the hydrophilic domains relative to that of pure water (μ^{∞}). The last term $\left(\frac{\phi_w}{\tau}\right)$ is the *tortuosity factor* that accounts for **(*iii*)** according to the tortuosity (τ) within the mesoscale network of hydrophilic domain volume (ϕ_w). A diffusion-in-pore model specifies the first term, and the second term is a Stokes-Einstein-type correction for viscosity using and the Einstein viscosity equation,[64] as shown in the SI. The reader is also referred to Reference 63 for complete model details. Using the experimentally-determined values for κ and ϕ_w, Equation (13) was solved for τ at each doping and hydration level.

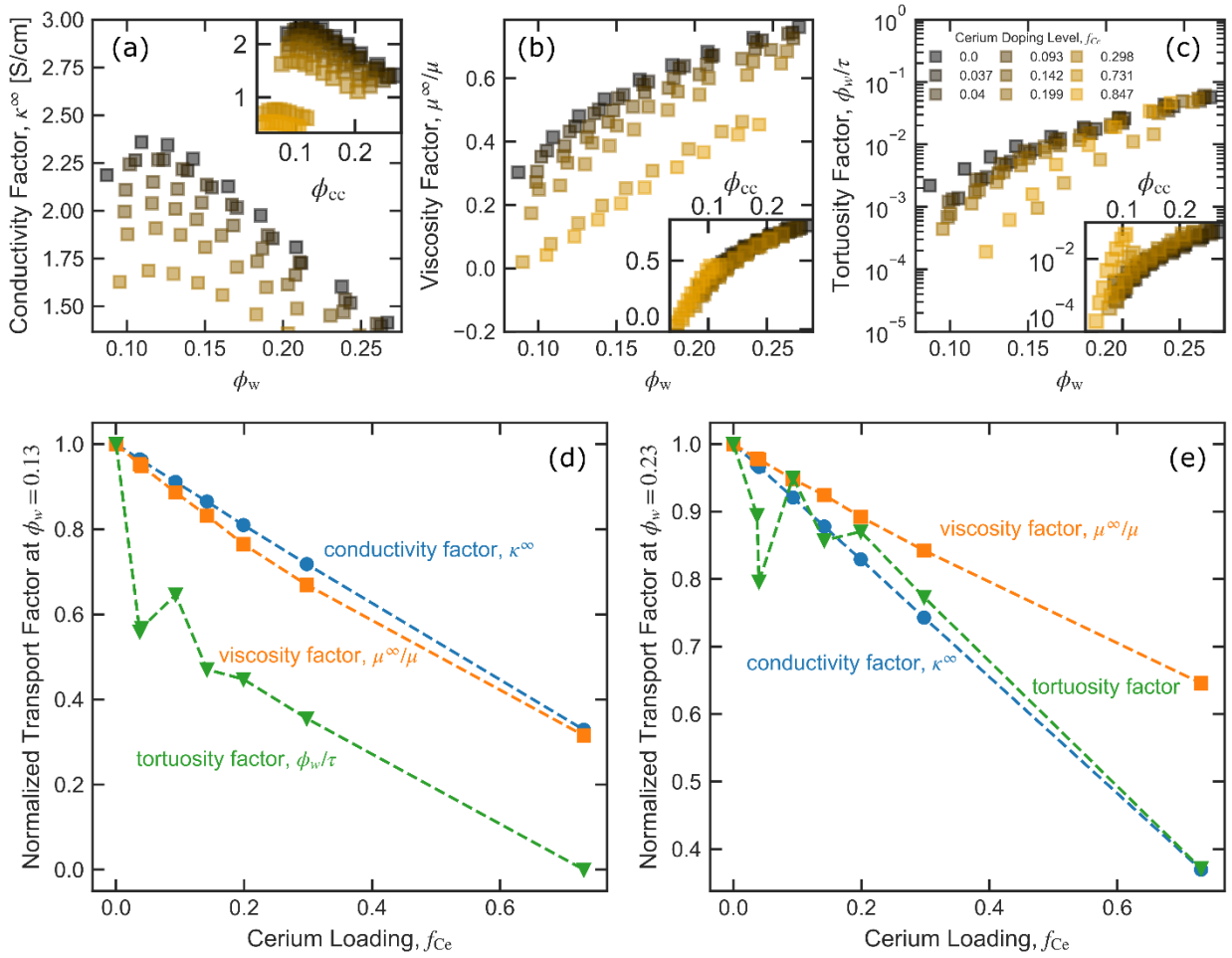

Figure 7 – Calculated transport factors for different Ce loadings (f_{Ce}) as a function of water volume fraction (ϕ_w): (a) the conductivity of PFSA-Ce^{Z+} without viscosity or tortuosity corrections, **(b)** the viscosity factor of the electrolyte solution inside the membrane, and **(c)** the tortuosity factor of hydrophilic domain network. Factors normalized to their proton forms are shown as a function of f_{Ce} for **(d)** ϕ_w = 0.1 and **(e)** ϕ_w = 0.2. The transport factors plotted as a function of the hydrated charge-carrier network volume fraction (ϕ_{cc}) are shown in the insets of **(a)-(c)**.

Figure 7a-c shows the contributions of the three calculated factors (***i-iii***) to the total macroscopic conductivity plotted as a function of ϕ_w. **Figure 7a** shows that as water is added to the membrane in proton form, the concentration of ionic groups decreases, which reduces the conductivity of a hypothetical solution in which cations have the same mobility as in infinite dilution (*i.e.*, constant water volume fraction and viscosity). Thus, accounting for (***i***), when Ce ions replace protons, the lower intrinsic mobility of Ce ions further reduces the ideal conductivity factor.

Figure 7b shows the viscosity factor (which is inversely proportional to viscosity of the electrolyte solution inside the membrane) also increases with hydration [Equations (S3) and (S4)], which increases conductivity according to Equation (13). Adding Ce ions increases viscosity at every hydration level (*i.e.*, shifts the viscosity factor curve down), in accordance with (***ii***). At the nanoscale, water strongly associates with the Ce ions independent of hydration (as shown in **Figure 2c**), which increases viscosity.[60]

Figure 7c shows that increasing the water volume fraction makes a larger fraction of the membrane conductive and increases connectivity between hydrophilic domains (*i.e.*, less tortuous mesoscale transport pathways) resulting in a larger tortuosity factor and higher conductivity. The addition of Ce ions decreases mesoscale domain connectivity (as shown in **Figure 6**), which results in a decreased tortuosity factor (*i.e.*, increased tortuosity) at a given hydration, decreasing conductivity as (***iii***) states.

Figure 7d and e show the transport factors normalized to their proton-form values at fixed low and high membrane hydration levels (ϕ_w = 0.1 and 0.2, respectively). This illustrates their relative influence on macroscale conductivity as a function of f_{Ce}. The assumption of this analysis, that electrolyte properties of the hydrophilic domains are similar to those of bulk electrolytes, is consistent with the findings of other studies.[65] At low hydration (**Figure 7d**), increased tortuosity causes the largest drop in conductivity relative to the contributions of proton displacement (reduced ideal conducitvity) and viscofication. At higher hydration (**Figure 7e**), both increased tortuosity and lower Ce ion mobility dominate the conductivity loss.

Interestingly, when these three factors are plotted as a function of ϕ_{cc} (**Figure 7, insets**), the parameter for charge-carrier network volume fraction, factors (***i-iii***) show different scaling trends, the combination of which yields the universal convergence of macroscopic conductivity with ϕ_{cc} (*i.e.*, $\kappa \propto \phi_{cc}$), as observed in **Figure 7b**. Next, we deconstruct the origins of this universality by analyzing how each factor scales with ϕ_{cc}. At a given ϕ_{cc}, (***i***) the conductivity factors *decreases* with f_{Ce} leading to downwards deviation from the scaling of macroscopic conductivity. (***ii***) The viscosity factors *converge* across all f_{Ce} and ϕ_{cc}, as it is directly governed by the volume fraction of hydrated charge carrier network, thereby matching the macroscopic scaling ($\kappa \propto \phi_{cc}$). Lastly, (***iii***) The tortuosity factors *increase* with f_{Ce} leading to upwards deviation from the macroscopic scaling. Hence, given that each factor directly contributes to the

macroscopic conductivity, their combination results in a net effect of matching the universal scaling of conductivity with the hydrated charge-carrier network volume fraction (*i.e.*, $\kappa \propto \phi_{cc}$.)

Recall that ϕ_{cc} is inversely proportional to f_{Ce} and proportional to RH (**Figure 2d**). Thus, the observation of increased tortuosity with increased f_{Ce} and decreased hydration follows the morphological changes inferred from SAXS data (**Figure 5**) and from previous hydration studies,[6,46,66] respectively. This establishes a qualitatively consistent link between the conductivity and tortuosity factors, even when analyzed in the context of ϕ_{cc}.

These findings corroborate the distinct role Ce doping plays at *nanoscales* (by changing ionic interactions and replacing protons with Ce ions of larger size/hydration number) and at *mesoscales* (through reduced concentrations of ionic charge carriers and increased tortuosity/heterogeneity of the hydrophilic domain network). Further, they give credence to using ϕ_{cc} for transport analysis, which mathematically accounts for the nanoscale and macroscale network effects by combining them in a newly defined term. This approach is beneficial for simplifying the analysis of transport properties of cation-ionomer systems; however, future studies should validate this approach in systems with varying/mixed cations and ionomer chemistries.

4.3 Implications for Migration/Diffusion

To illustrate the role Ce ions play in these devices, we considered an isothermal, 1-D cell model consisting of a membrane sandwiched between two Pt metal electrodes that form a hydrogen pump (*i.e.*, hydrogen oxidation and evolution), the details of which are described in the SI. In this example, the chemical potential of water is uniform across the membrane. A current density (i) is applied to the cell that is proportional to the proton flux at steady state. Here, the flux of Ce in the membrane (N_{Ce}) is zero because it cannot leave the membrane.[67] Concentrated-solution theory dictates that species fluxes are related to i and chemical potential gradients of Ce and protons (μ_{Ce} and μ_H, respectively):[68,69]

$$N_{Ce} = 0 = \frac{t_{Ce} i}{z_{Ce} F} - \alpha_{Ce} \frac{d}{dx}\left(\mu_{Ce} - \frac{z_{Ce}}{z_H}\mu_H\right) \quad (14)$$

where F is the Faraday constant and t_{Ce} is the transference number of Ce. α_{Ce} is a transport coefficient that describes the flux of Ce ions under Ce and proton ionic chemical potential gradients:

$$\alpha_{\mathrm{Ce}} = \alpha_{\mathrm{Ce}}^{\infty}\left(\frac{\mu^{\infty}}{\mu}\right)\left(\frac{\phi_w}{\tau}\right) \tag{15}$$

which is, notably, dependent on viscosity ($\frac{\mu^{\infty}}{\mu}$) and tortuosity $\left(\frac{\phi_w}{\tau}\right)$ terms.

Equation (14) shows that at steady-state in an electrochemical cell, migration (first term) is balanced by Ce diffusion down the Ce and up the H^+ chemical potential gradients (second term). The microscale model used to specify conductivity is based on a molecular description of Stefan-Maxwell friction coefficients that allows self-consistent calculation of any other membrane transport properties.[63] This model has been validated against various systems,[63] and the gradients predicted (**Figure S6**) match both the direction and shape of those experimentally-observed using microprobe and benchtop XRF.[27,30] With this in mind, their precision would be refined through further validation, but their outputs are qualitatively accurate. Similarly to the conductivity model, the experimentally-determined values for κ and ϕ_w and the microscale models for $\alpha_{\mathrm{Ce}}^{\infty}$ and t_{Ce} were used to solve Equation (14) for τ at each doping and hydration level.

Figure 8 plots the resulting (a) α_{Ce} and (b) t_{Ce} as a function of f_{Ce} and ϕ_w. This approach contrasts previous transport studies, where Ce migration coefficients were taken to be independent of f_{Ce}.[3,27,30] At high ϕ_w (blue circles), as f_{Ce} increases, α_{Ce} and t_{Ce} both increase because there are additional Ce ions to diffuse and carry current. At low ϕ_w (orange squares), α_{Ce} is significantly reduced relative to the high ϕ_w case as the hydrophilic network becomes more tortuous and impedes transport. This is consistent with the order-of-magnitude decrease in tortuosity factor modeled at low ϕ_w (**Figure 7a**), which dominates the α_{Ce} term. Since t_{Ce} is independent of these tortuosity and viscosity factors, its behavior is similar at low and high ϕ_w. These trends are consistent across all ϕ_{w} measured, which underscores the importance of considering f_{Ce} when determining cation transport coefficients, especially at ϕ_w and f_{Ce}, which may result in α_{Ce} variations of greater than two orders of magnitude relative to the proton form (**Figure S7a**).

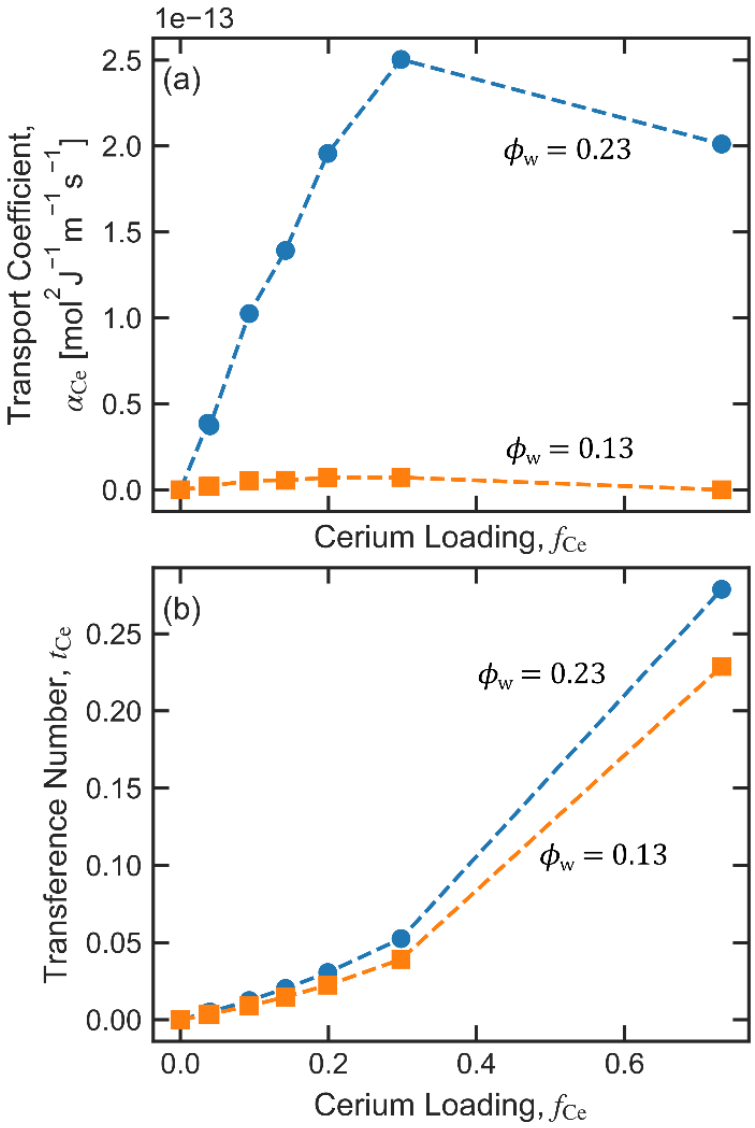

Figure 8 – The **(a)** transport coefficient (α_{Ce}) and **(b)** transference number (t_{Ce}) of Ce^{3+} as a function of different Ce loadings (f_{Ce}) at low and high water volume fractions (ϕ_w = 0.13 and 0.23, respectively). Values for all ϕ_w are shown in **Figure S7**.

In electrochemical devices, Ce ions create mass-transport limitations by preventing protons from reaching the cathode,[37,38,70] plus indirectly induces them increasing the viscosity and tortuosity of the hydrophilic domains in the membrane (**Figure 7**) which decreases proton and Ce transport coefficients (**Figure 8**). To highlight the importance of the Ce-dependent hydration and transport properties reported in this work on membrane performance, the membrane behavior is simulated for various scenarios.

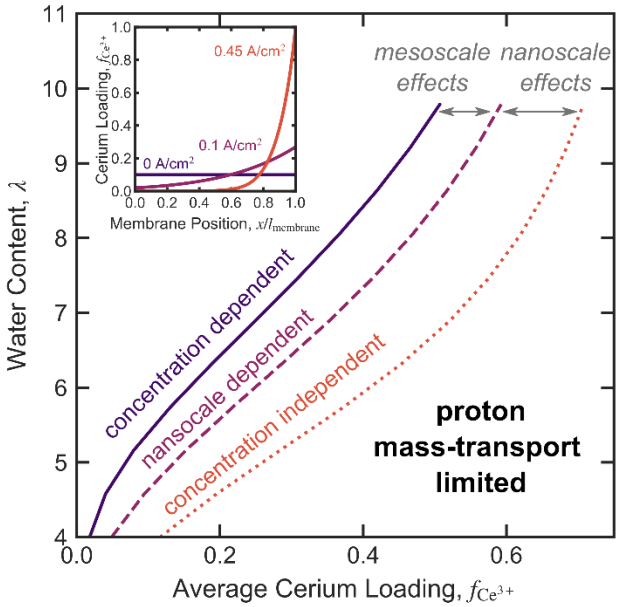

Figure 9 – Maximum membrane Ce loading (f_{Ce}) and minimum average water content (λ) allowed to maintain a proton mass-transport limiting current of 0.1 A/cm^2 in a proton pump simulated under 3 scenarios: without accounting for Ce ion impacts on nanoscale viscosity or mesoscale tortuosity [dotted line, using Equation (16)], depending on only nanoscale effects of Ce ions [dashed line, using Equation (17)], and fully dependent on Ce ion contents [solid line, using Equation (15)].

Figure 9 shows the average membrane Ce loading and water content at which the mass-transport limited current density becomes 0.1 A/cm^2 for different scenarios of how Ce transport coefficient, α_{Ce}, depends on f_{Ce}. When α_{Ce} does not incorporate how f_{Ce} changes hydrophilic domain viscosity or tortuosity, it is simplified to:

$$\alpha_{\mathrm{Ce}} = \alpha_{\mathrm{Ce}}^{\infty}\left(\frac{\mu^{\infty}}{\mu}\right)_{f_{\mathrm{Ce^{3+}=0}}}\left(\frac{\phi_w}{\tau}\right)_{f_{\mathrm{Ce^{3+}=0}}} \tag{16}$$

The dotted line in **Figure 9** shows that in this scenario, relatively high f_{Ce} and low λ are possible before reaching a 0.1 A/cm^2 limiting current, suggesting a rather positive scenario. Including only the nanoscale impact that Ce has on the hydrophilic domain viscosity, the Ce transport coefficient becomes:

$$\alpha_{\mathrm{Ce}} = \alpha_{\mathrm{Ce}}^{\infty}\left(\frac{\mu^{\infty}}{\mu}\right)\left(\frac{\phi_w}{\tau}\right)_{f_{\mathrm{Ce^{3+}=0}}} \tag{17}$$

which reduces the transport coefficient and causes mass-transport limiting currents at a higher λ and lower f_{Ce} relative to the concentration-independent case, as shown by the dashed line in **Figure**

9. When Ce content impacts the transport coefficient by changing both tortuosity and viscosity of the hydrophilic domains Equation (15) may be used to calculate α_{Ce}. As shown by the solid line in **Figure 9**, in this scenario, the cell must be wet and have relatively low f_{Ce} to reach the same level of current. These results indicate that using Ce-independent properties and not accounting for local increases in Ce contents (despite an average low f_{Ce}) would provide a misleading picture for the actual resistances occurring in a membrane. The changes Ce ions have on the nano- and mesoscales impacts cell performance to a similar extent, which highlights the key roles that cations play in both local changes in solvation and viscosity, as well as structural changes occurring at longer length scales, including the phase-separation, and ionic crosslinks, which affect domain network morphology.

4.4 Summary of Changes in Properties

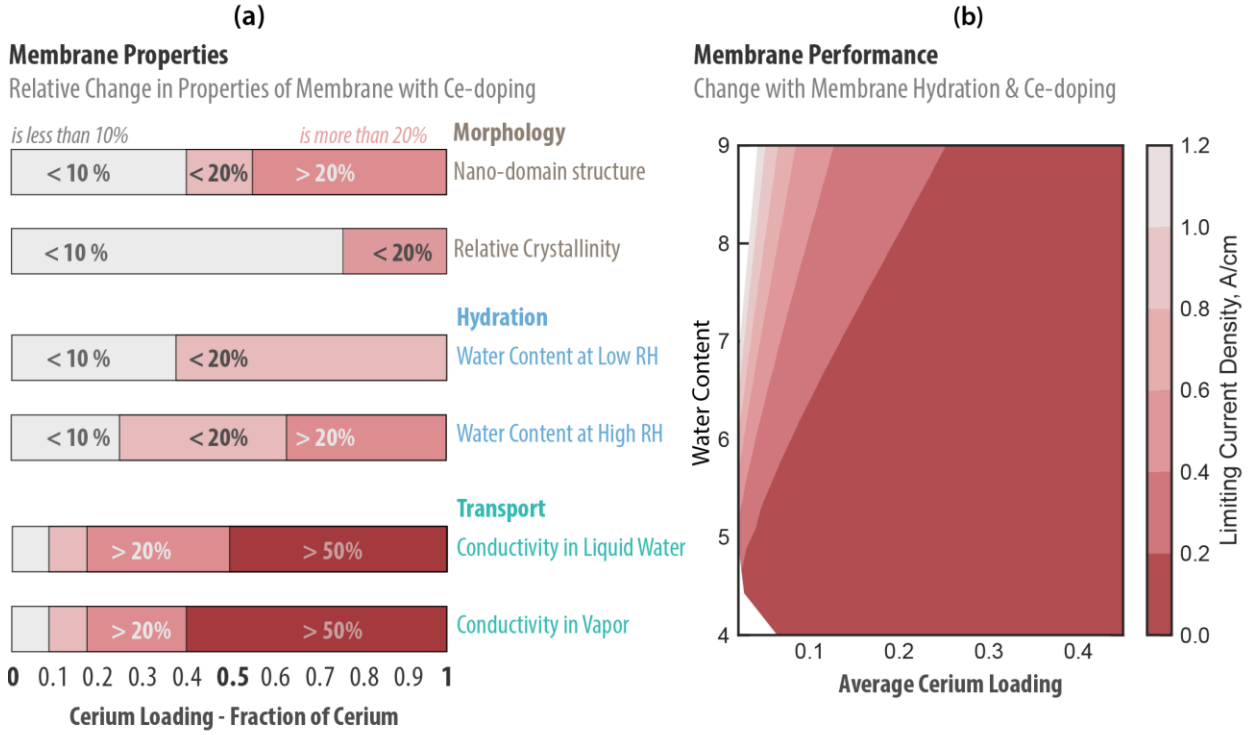

Figure 10 – **Implication of Ce doping (a) membrane's properties and (b) cell performance. (a)** The ranges of Ce-exchange percentage (f_{Ce}) in PFSA-Ce^{Z+} membranes over which membrane properties change less than 10%, between 10 and 20%, and over 20 and 50%, relative to those for the protonated form (f_{Ce} = 0). The ranges are estimated based on the data reported in this paper and shown solely to highlight the relative impact of Ce loading on selected structural and transport properties, and therefore should not be taken as a definitive guidance for ionomer membranes. **(b)** A contour map of mass-transport limiting current density in the membrane as a function of membrane water content and Ce loading calculated by numerically integrating Equation (14) across the membrane thickness.

To illustrate the changes in the membrane structural, hydration, and transport properties incurred by Ce doping, the measured data were analyzed to identify approximately how much Ce should be exchanged in a PFSA membrane to induce a prescribed reduction in membrane properties, relative to the protonated form. **Figure 10a** demonstrates the ranges of Ce doping within which relative change of a property is less than 10%, 20%, and over 20%. Six properties were chosen to represent the structure-property relationship of the membrane and despite variation among the measurement conditions, the diagram nevertheless provides guidance for qualitative changes expected in membranes with Ce doping. The implications of these changes in hydration and transport properties on cell performance are also analyzed using the model to determine the proton mass-transport limiting current as a function of Ce loading and membrane water content. **Figure 10b** shows a contour plot of the limiting current density, which sharply decreases with a small amount of Ce doping. This impact is exacerbated in dry conditions in which the cell can tolerate only slight Ce loadings. Consequently, there is a tradeoff between operating in dry conditions and high Ce loadings. It must be noted that ionomer's behavior in the entire Ce doping range is important and relevant, even if the initial average loading is low, because of the significant in-plane[32] and through-plane[26] changes to the local concentrations due cation transport during device operation.

Interestingly, even with over 50% Ce ion doping ($f_{\mathrm{Ce}} > 0.5$), most nanostructural changes and reductions in water uptake are less than 20%. The fact that nanoscale domain spacing and water content exhibit similar relative changes with Ce exchange underscores the universal correlation between structure and swelling in ionomers and how it is maintained in membrane systems with controlled levels of cation dopants. A notable exception to this trend is the conductivity, which exhibits a more dramatic reduction with increased Ce doping: a 20% decrease is induced for less than 20% doping ($f_{\mathrm{Ce}} < 0.2$), while conductivity decreases by half once the doping levels reach 50% ($f_{\mathrm{Ce}} = 0.5$). This demonstrates the complex nature of ion transport in PFSA of mixed cations, which is governed by nanostructure and hydration, and also by multiscale structural effects, cation solvation, and cation-anion interactions, ultimately yielding a nonlinear trend. In fact, because a universal correlation between conductivity and hydration is found only when hydration is characterized by volume fraction of water adjusted for ion fraction in the

membrane instead of per anion, the key role of cation solvation and cation-water interactions is supported. The interplay between these factors may explain the variation in conductivity trends experimentally observed for other PFSA-cation systems.[42]

Furthermore, while Ce exchange affects the hydrophilic domains at nanoscales, it also impacts morphological reorganization that can be associated with tortuosity and network effects, which are shown to have negative implications for membrane's transport resistance. These features, therefore, correspond to conductivity diminished disproportionately with doping level, compared to that expected by simple substitution of protons by less mobile Ce, alone. The impact of Ce loading on membrane properties increases in the order of hydration < morphology < transport, with over 25% decrease in conductivity at a loading exceeding $f_{\mathrm{Ce}} > 0.25$, yet the convoluted impact of these changes on cell performance is even more severe, with over 100% reduction in limiting current, especially during dry operation. While a membrane containing less Ce and more water could mitigate some of these performance losses, considering the realistic cell operating conditions and Ce loading range for commercially-feasible durable membranes, the impact of Ce on cell performance limitation is evident with an apparent performance-durability interplay.

5. Conclusions

The importance of PFSAs in electrochemical technologies makes it a critical target for analysis. In particular, the study of cation-poly(anion) complexes used in PFSA to neutralize radicals is necessary to better understand their transport mechanisms and overall impact on performance. The studies performed help elucidate those phenomena. Water-uptake measurements indicate that with increased Ce ion doping, water uptake increases at lower RH and decreases at higher RH levels. Liquid-water conductivity measurements show that conductivity decreases with increased Ce doping. This effect is exacerbated in vapor conditions, where Ce cations negatively affect proton transport the most under hot and dry conditions. SAXS data reveal a broader ionomer scattering peak with increasing Ce doping, suggesting a weaker degree of phase-separation between hydrophobic and hydrophilic domains.

The relationship between conductivity and hydration was further explored, and a universal correlation was defined based on the hydrated charge carrier network volume fraction. Modeling of transport mechanisms also suggest conductivity diminishes disproportionately with doping level, compared to that expected by simple substitution of protons by less mobile Ce, which underscores the critical role of multiscale structural changes in the ionomer system, and also provides the basis for further studies on how these findings can be applied to other mixed cation systems. Also, because of Ce gradients forming within the membrane, low average Ce loadings can cause high local Ce concentrations, which highlights the importance of measuring and using Ce-dependent properties with a wide range of doping levels, even if the initial doping in the membrane is low. The combined experimental and theoretical analysis demonstrate a nonlinear decrease in conductivity driven by cation solvation at the nanoscale and morphological changes at longer length scales, with strong implications on cation transport and cell performance, which are used to guide design of fuel cell membranes with optimized functionality and performance.

Supporting Information

The SI contains Ce ion doping calibration curves and corresponding levels of total cations measured in these experiments; conductivity data across a range of T/RHs; SAXS/WAXS spectra and fitting procedures, along with crystallinity results; conductivity model details; transport model details and calculated 1-D cation profiles in the membrane during device operation with corresponding transport coefficients and transference numbers.

Acknowledgments

This research is supported by the U.S. Department of Energy Fuel Cell Technologies Office, through the Fuel Cell Performance and Durability (FC-PAD) Consortium (Fuel Cells Program Manager: Greg Kleen, Dimitrios Papageorgopoulos). This work also made use of facilities at the Advanced Light Source Beamline 7.3.3, supported by the Office of Science, Office of Basic Energy Sciences, of the U.S. Department of Energy (Contract No. DE-AC02-05CH11231).

References

(1) Perry, M. L.; Weber, A. Z. Advanced Redox-Flow Batteries: A Perspective. *J. Electrochem. Soc.* **2016**, *163* (1), 5064–5067. https://doi.org/10.1149/2.0101601jes.

(2) Zatoń, M.; Prélot, B.; Donzel, N.; Rozière, J.; Jones, D. J. Migration of Ce and Mn Ions in PEMFC and Its Impact on PFSA Membrane Degradation. *J. Electrochem. Soc.* **2018**, *165* (6), F3281–F3289. https://doi.org/10.1149/2.0311806jes.

(3) Cai, Y.; Ziegelbauer, J. M.; Baker, A. M.; Gu, W.; Kukreja, R. S.; Kongkanand, A.; Mathias, M. F.; Mukundan, R.; Borup, R. L. Electrode Edge Cobalt Cation Migration in an Operating Fuel Cell: An In Situ Micro-X-Ray Fluorescence Study. *J. Electrochem. Soc.* **2018**, *165* (6), F3132–F3138. https://doi.org/10.1149/2.0201806jes.

(4) Coms, F. D.; Fuller, T. J.; Schaffer, C. P. A Mechanistic Study of Perfluorosulfonic Acid Membrane Water Permeance Degradation in Air. *J. Electrochem. Soc.* **2018**, *165* (6), 3104–3110. https://doi.org/10.1149/2.0141806jes.

(5) Okada, T. Effect of Ionic Contaminants. In *Handbook of Fuel Cells*; John Wiley & Sons, 2010. https://doi.org/10.1002/9780470974001.f303054.

(6) Kusoglu, A.; Weber, A. Z. New Insights into Perfluorinated Sulfonic-Acid Ionomers. *Chem. Rev.* **2017**, *117* (3), 987–1104. https://doi.org/10.1021/acs.chemrev.6b00159.

(7) Coms, F. D. The Chemistry of Fuel Cell Membrane Chemical Degradation. *ECS Trans.* **2008**, *16* (2), 235–255. https://doi.org/10.1149/1.2981859.

(8) Gubler, L.; Dockheer, S. M.; Koppenol, W. H. Radical (HO●, H● and HOO●) Formation and Ionomer Degradation in Polymer Electrolyte Fuel Cells. *J. Electrochem. Soc.* **2011**, *158* (7), B755–B769. https://doi.org/10.1149/1.3581040.

(9) Rodgers, M. P.; Bonville, L. J.; Kunz, H. R.; Slattery, D. K.; Fenton, J. M. Fuel Cell Perfluorinated Sulfonic Acid Membrane Degradation Correlating Accelerated Stress Testing and Lifetime. *Chem. Rev.* **2012**, *112* (11), 6075–6103. https://doi.org/10.1021/cr200424d.

(10) Hommura, S.; Kawahara, K.; Shimohira, T.; Teraoka, Y. Development of a Method for Clarifying the Perfluorosulfonated Membrane Degradation Mechanism in a Fuel Cell Environment. *J. Electrochem. Soc.* **2007**, *155* (1), A29–A33. https://doi.org/10.1149/1.2800171.

(11) F. D. Coms, H. Xu, T. McCallum, C. M. Mechanism of Perfluorsulfonic Acid Membrane Chemical Degradation Under Low RH Conditions F. D. Coms. *ECS Trans.* **2012**, *50* (2), 907–918. https://doi.org/10.1149/06403.0389ecst.

(12) Xu, H.; Borup, R. L.; Brosha, E.; Gazon, F.; Pivovar, B. S. Effect of Relative Humidity on Membrane Degradation Rate and Mechanism in PEM Fuel Cells. *ECS Trans.* **2007**, *6* (13), 51–62. https://doi.org/10.1149/1.2811696.

(13) Mukundan, R.; Baker, A. M.; Kusoglu, A.; Beattie, P.; Knights, S.; Weber, A. Z.; Borup, R. L. Membrane Accelerated Stress Test Development for Polymer Electrolyte Fuel Cell Durability Validated Using Field and Drive Cycle Testing. *J. Electrochem. Soc.* **2018**, *165* (6), F3085–F3093. https://doi.org/10.1149/2.0101806jes.

(14) Wong, K. H.; Kjeang, E. Simulation of Performance Tradeoffs in Ceria Supported Polymer Electrolyte Fuel Cells. *J. Electrochem. Soc.* **2019**, *166* (2), F128–F136. https://doi.org/10.1149/2.0771902jes.

(15) Ehlinger, V. M.; Kusoglu, A.; Weber, A. Z. Modeling Coupled Durability and Performance in Polymer-Electrolyte Fuel Cells: Membrane Effects. *J. Electrochem. Soc.* **2019**, *166* (7), F3255–F3267. https://doi.org/10.1149/2.0281907jes.

(16) Gittleman, C. S.; Coms, F. D.; Lai, Y. H. Membrane Durability: Physical and Chemical Degradation. In *Polymer Electrolyte Fuel Cell Degradation*; Mench, M. M., Caglan Kumbur, E., Veziroglu, T. N., Eds.; Elsevier Science: Burlington, 2011. https://doi.org/10.1016/B978-0-12-386936-4.10002-8.

(17) Kreitmeier, S.; Lerch, P.; Wokaun, A.; Büchi, F. N. Local Degradation at Membrane Defects in Polymer Electrolyte Fuel Cells. *J. Electrochem. Soc.* **2013**, *160* (4), F456–F463. https://doi.org/10.1149/1.023306jes.

(18) Lim, C.; Ghassemzadeh, L.; Van Hove, F.; Lauritzen, M.; Kolodziej, J.; Wang, G. G.; Holdcroft, S.; Kjeang, E. Membrane Degradation during Combined Chemical and Mechanical Accelerated Stress Testing of Polymer Electrolyte Fuel Cells. *J. Power Sources* **2014**, *257*, 102–110. https://doi.org/10.1016/j.jpowsour.2014.01.106.

(19) Weber, A. Z.; Borup, R. L.; Darling, R. M.; Das, P. K.; Dursch, T. J.; Gu, W.; Harvey, D.; Kusoglu, A.; Litster, S.; Mench, M. M.; et al. A Critical Review of Modeling Transport Phenomena in Polymer-Electrolyte Fuel Cells. **2014**, *161* (12), 1254–1299. https://doi.org/10.1149/2.0751412jes.

(20) Trogadas, P.; Parrondo, J.; Ramani, V. Degradation Mitigation in Polymer Electrolyte Membranes Using Cerium Oxide as a Regenerative Free-Radical Scavenger. *Electrochem. Solid-State Lett.* **2008**, *11* (7), B113–B116. https://doi.org/10.1149/1.2916443.

(21) Pearman, B. P.; Mohajeri, N.; Brooker, R. P.; Rodgers, M. P.; Slattery, D. K.; Hampton, M. D.; Cullen, D. A.; Seal, S. The Degradation Mitigation Effect of Cerium Oxide in Polymer Electrolyte Membranes in Extended Fuel Cell Durability Tests. *J. Power Sources* **2013**, *225*, 75–83. https://doi.org/10.1016/j.jpowsour.2012.10.015.

(22) Wang, L.; Advani, S. G.; Prasad, A. K. Degradation Reduction of Polymer Electrolyte Membranes Using CeO2 as a Free-Radical Scavenger in Catalyst Layer. *Electrochim. Acta* **2013**, *109*, 775–780. https://doi.org/10.1016/j.electacta.2013.07.189.

(23) Gubler, L.; Koppenol, W. H. Kinetic Simulation of the Chemical Stabilization Mechanism in Fuel Cell Membranes Using Cerium and Manganese Redox Couples. *J. Electrochem. Soc.* **2012**, *159* (2), B211–B218. https://doi.org/10.1149/2.075202jes.

(24) Okada, T.; Xie, G.; Gorseth, O.; Kjelstrup, S.; Nakamura, N.; Arimura, T. Ion and Water Transport Characteristics of Nafion Membranes as Electrolytes. *Electrochim. Acta* **1998**, *43* (24), 3741–3747. https://doi.org/10.1016/S0013-4686(98)00132-7.

(25) Kienitz, B. L.; Baskaran, H.; Zawodzinski, T. A. Modeling the Steady-State Effects of Cationic Contamination on Polymer Electrolyte Membranes. *Electrochim. Acta* **2009**, *54* (6), 1671–1679. https://doi.org/10.1016/j.electacta.2008.09.058.

(26) Baker, A. M.; Cai, Y.; Ziegelbauer, J. M.; Agyeman-Budu, D.; Woll, A.; Kongkanand, A.;

Mukundan, R.; Borup, R. L. Development of Operando Confocal Microprobe X-Ray Fluorescence Techniques to Measure Cation Transport in PEM Fuel Cells. *ECS Trans.* **2019**, *92* (8), 107–117. https://doi.org/10.1149/09208.0107ecst.

(27) Baker, A. M.; Komini Babu, S.; Chintam, K.; Kusoglu, A.; Mukundan, R.; Borup, R. L. Ce Cation Migration and Diffusivity in Perfluorosulfonic Acid Fuel Cell Membranes. *ECS Trans.* **2019**, *92* (8), 429–438. https://doi.org/10.1149/09208.0429ecst.

(28) Goswami, A.; Acharya, A.; Pandey, A. K. Study of Self-Diffusion of Monovalent and Divalent Cations in Nafion-117 Ion-Exchange Membrane. *J. Phys. Chem. B* **2001**, *105*, 9196–9201. https://doi.org/10.1021/jp010529y.

(29) Coms, F. D.; McQuarters, A. B. Determination of Ce3+ and Co2+ Diffusion Coefficients in NR211 Membrane. *ECS Trans.* **2018**, *86* (13), 395–405. https://doi.org/10.1149/08613.0395ecst.

(30) Baker, A. M.; Babu, S. K.; Mukundan, R.; Advani, S. G.; Prasad, A. K.; Spernjak, D.; Borup, R. L. Cerium Ion Mobility and Diffusivity Rates in Perfluorosulfonic Acid Membranes Measured via Hydrogen Pump Operation. *J. Electrochem. Soc.* **2017**, *164* (12), 1272–1278. https://doi.org/10.1149/2.1221712jes.

(31) Baker, A. M.; Mukundan, R.; Spernjak, D.; Judge, E. J.; Advani, S. G.; Prasad, A. K.; Borup, R. L. Cerium Migration during PEM Fuel Cell Accelerated Stress Testing. *J. Electrochem. Soc.* **2016**, *163* (9), F1023–F1031. https://doi.org/10.1149/2.0181609jes.

(32) Lai, Y.-H.; Rahmoeller, K. M.; Hurst, J. H.; Kukreja, R. S.; Atwan, M.; Maslyn, A. J.; Gittleman, C. S. Accelerated Stress Testing of Fuel Cell Membranes Subjected to Combined Mechanical/Chemical Stressors and Cerium Migration. *J. Electrochem. Soc.* **2018**, *165* (6), F3217–F3229. https://doi.org/10.1149/2.0241806jes.

(33) Baker, A. M.; Torraco, D.; Judge, E. J.; Spernjak, D.; Mukundan, R.; Borup, R. L.; Advani, S. G.; Prasad, A. K. Cerium Migration during PEM Fuel Cell Assembly and Operation. In *ECS Meeting Abstracts*; 2015; p 1495. https://doi.org/10.1149/MA2015-02/37/1495.

(34) Baker, A. M.; Williams, S. T. D.; Mukundan, R.; Spernjak, D.; Advani, S. G.; Prasad, A. K.; Borup, R. L. Zr-Doped Ceria Additives for Enhanced PEM Fuel Cell Durability and Radical Scavenger Stability. *J. Mater. Chem. A* **2017**, *5*, 15073–15079. https://doi.org/10.1039/C7TA03452K.

(35) Stewart, S. M.; Spernjak, D.; Borup, R.; Datye, A.; Garzon, F. Cerium Migration through Hydrogen Fuel Cells during Accelerated Stress Testing. *ECS Electrochem. Lett.* **2014**, *3* (4), F19–F22. https://doi.org/10.1149/2.008404eel.

(36) Wong, K. H.; Kjeang, E. In-Situ Modeling of Chemical Membrane Degradation and Mitigation in Ceria-Supported Fuel Cells. *J. Electrochem. Soc.* **2017**, *164* (12), F1179–F1186. https://doi.org/10.1149/2.1201712jes.

(37) Dumont, J. H.; Baker, A. M.; Maurya, S.; Kim, Y. S.; Mukundan, R.; Borup, R. L. Effect of Cerium, Cobalt and Nickel Contaminants on the Oxygen Reduction Reaction at Platinum Electrodes. *ECS Trans.* **2017**. https://doi.org/10.1149/08008.0861ecst.

(38) Banham, D.; Ye, S.; Knights, S.; Stewart, S. M.; Wilson, M.; Garzon, F. UV-Visible Spectroscopy Method for Screening the Chemical Stability of Potential Antioxidants for Proton Exchange Membrane Fuel Cells. *J. Power Sources* **2015**, *281*, 238–242. https://doi.org/10.1016/j.jpowsour.2015.02.002.

(39) Bontha, J. R.; Pintauro, P. N. Water Orientation and Ion Solvation Effects during Multicomponent Salt Partitioning in a Nafion Cation Exchange Membrane. *Chem. Eng. Sci.* **1994**, *49* (23), 3835–3851. https://doi.org/10.1016/0009-2509(94)00205-3.

(40) Tandon, R.; Pintauro, P. N. Divalent/Monovalent Cation Uptake Selectivity in a Nafion Cation-Exchange Membrane: Experimental and Modeling Studies. *J. Memb. Sci.* **1997**, *136* (1–2), 207–219. https://doi.org/10.1016/S0376-7388(97)00167-1.

(41) Okada, T.; Møller-holst, S.; Gorseth, O.; Kjelstrup, S. Transport and Equilibrium Properties of Nafion Membranes with H+ and Na+ Ions. *J. Electroanal. Chem.* **1998**, *442*, 137–145. https://doi.org/10.1016/S0022-0728(97)00499-3.

(42) Okada, T.; Ayato, Y.; Yuasa, M.; Sekine, I. The Effect of Impurity Cations on the Transport Characteristics of Perfluorosulfonated Ionomer Membranes. *J. Phys. Chem. B* **1999**, *103*, 3315–3322. https://doi.org/10.1021/jp983762d.

(43) Yang, Y.; Pintauro, P. N. Multicomponent Space-Charge Transport Model for Ion-Exchange Membranes. *AIChE J.* **2000**, *46* (6), 1177–1190. https://doi.org/10.1021/ie030558q.

(44) Saito, M.; Arimura, N.; Hayamizu, K.; Okada, T. Mechanisms of Ion and Water Transport in Perfluorosulfonated Ionomer Membranes for Fuel Cells. *J. Phys. Chem. B* **2004**, *108*, 16064–16070. https://doi.org/10.1021/jp0482565.

(45) Goodwin, J. G.; Hongsirikarn, K.; Greenway, S.; Creager, S. Effect of Cations (Na+, Ca2+, Fe3+) on the Conductivity of a Nafion Membrane. *J. Power Sources* **2010**, *195* (21), 7213–7220. https://doi.org/10.1016/j.jpowsour.2010.05.005.

(46) Shi, S.; Weber, A. Z.; Kusoglu, A. Structure-Transport Relationship of Perfluorosulfonic-Acid Membranes in Different Cationic Forms. *Electrochim. Acta* **2016**, *220*, 517–528. https://doi.org/10.1016/j.electacta.2016.10.096.

(47) Redmond, E. L.; Wriston, S. M.; Szarka III, J. L. Full Factorial Experiment to Determine and Predict Impact of Cerium Amount on Fuel Cell Performance. *ECS Trans.* **2017**, *80* (8), 633–641. https://doi.org/10.1149/08008.0633ecst.

(48) Coms, F. D.; Liu, H.; Owejan, J. E. Mitigation of Perfluorosulfonic Acid Membrane Chemical Degradation Using Cerium and Manganese Ions. *ECS Trans.* **2008**, *16* (2), 1735–1747. https://doi.org/10.1149/1.2982015.

(49) Shibata, M.; Kitano, N.; Shinohara, A.; Asaoka, T.; Sekine, S.; Takeuchi, N.; Morita, T.; Kumei, H. Estimation of Cation Contamination Level in Polymer Electrolyte Membrane Fuel Cells by Electrochemical Impedance Spectroscopy. *ECS Trans.* **2018**, *85* (13), 905–926. https://doi.org/10.1149/08513.0905ecst.

(50) Peng, J.; Tian, M.; Cantillo, N. M.; Zawodzinski, T. The Ion and Water Transport Properties of K+ and Na+ Form Perfluorosulfonic Acid Polymer. *Electrochim. Acta* **2018**, *282*, 544–554. https://doi.org/10.1016/j.electacta.2018.06.035.

(51) Shi, S.; Weber, A. Z.; Kusoglu, A. Structure/Property Relationship of Nafion XL Composite Membranes. *J. Memb. Sci.* **2016**, *516*, 123–134. https://doi.org/10.1016/j.memsci.2016.06.004.

(52) Cooper, K. R. Progress Toward Accurate Through-Plane Ion Transport Resistance Measurement of Thin Solid Electrolytes. *J. Electrochem. Soc.* **2010**, *157* (11), B1731. https://doi.org/10.1149/1.3481561.

(53) Kusoglu, A.; Savagatrup, S.; Clark, K. T.; Weber, A. Z. Role of Mechanical Factors in Controlling the Structure − Function Relationship of PFSA Ionomers. *Macromolecules* **2012**, *45* (18), 7467–7476. https://doi.org/10.1021/ma301419s.

(54) Lutz, O. M. D.; Hofer, T. S.; Randolf, B. R.; Rode, B. M. Computational Study of the Cerium(III) Ion in Aqueous Environment. *Chem. Phys. Lett.* **2012**, *539–540*, 50–53. https://doi.org/10.1016/j.cplett.2012.05.023.

(55) Swanson, J. M. J.; Maupin, C. M.; Chen, H.; Petersen, M. K.; Xu, J.; Wu, Y.; Voth, G. A. Proton Solvation and Transport in Aqueous and Biomolecular Systems : Insights From. **2020**, 4300–4314. https://doi.org/10.1021/jp070104x.

(56) Cui, S.; Paddison, S. J. A Molecular Dynamics Study of the Effects of V 2+ and V 3+ on the Local Structure of Hydrated Nafion. *J. Phys. Chem. C* **2015**, *119*, 12848–12855. https://doi.org/10.1021/acs.jpcc.5b02876.

(57) Xie, G.; Okada, T. Water Transport Behavior in Nation 117 Membranes. *J. Electrochem. Soc.* **1995**, *142* (9), 3057–3062. https://doi.org/10.1149/1.2048686.

(58) Lai, Y.; Fly, G. W. In-Situ Diagnostics and Degradation Mapping of a Mixed-Mode Accelerated Stress Test for Proton Exchange Membranes. *J. Power Sources* **2015**, *274*, 1162–1172. https://doi.org/10.1016/j.jpowsour.2014.10.116.

(59) Su, G. M.; Cordova, I. A.; Yandrasits, M. A.; Lindell, M.; Feng, J.; Wang, C.; Kusoglu, A. Chemical and Morphological Origins of Improved Ion Conductivity in Perfluoro Ionene Chain Extended Ionomers. *J. Am. Chem. Soc.* **2019**, *141* (34), 13547–13561. https://doi.org/10.1021/jacs.9b05322.

(60) Crothers, A. R.; Radke, C. J.; Weber, A. Z. Impact of Nano- and Mesoscales on Macroscopic Cation Conductivity in Perfluorinated-Sulfonic-Acid Membranes. *J. Phys. Chem. C* **2017**, *121* (51), 28262–28274. https://doi.org/10.1021/acs.jpcc.7b07360.

(61) Okada, T.; Nakamura, N.; Yuasa, M.; Sekine, I. Ion and Water Transport Characteristics in Membranes for Polymer Electrolyte Fuel Cells Containing H+ and Ca2+ Cations. *J. Electrochem. Soc.* **1997**, *144* (8), 2744–2750. https://doi.org/10.1149/1.1837890.

(62) *CRC Handbook of Chemistry and Physics*; CRC Press: Cleveland, Ohio, 1978.

(63) Crothers, A. R.; Darling, R. M.; Radke, C. J.; Weber, A. Z.; Soc, J. E.; Crothers, A. R.; Darling, R. M.; Kusoglu, A.; Radke, C. J.; Weber, A. Z. Theory of Multicomponent

Phenomena in Cation-Exchange Membranes, II: Transport Model and Validation. *J. Electrochem. Soc.* **2020**, *167*, 013548. https://doi.org/10.1149/1945-7111/ab6724.

(64) Hiemenz, P. C. *Principles of Colloid and Surface Chemistry*; Marcel Dekker: New York.

(65) Lingwood, M. D.; Zhang, Z.; Kidd, B. E.; Mccreary, K. B. Unraveling the Local Energetics of Transport in a Polymer Ion Conductor. *Chem. Commun.* **2013**, *48*, 4283–4285. https://doi.org/10.1039/c2cc37173a.

(66) Zhao, Q.; Majsztrik, P.; Benziger, J. Diffusion and Interfacial Transport of Water in Nafion. *J. Phys. Chem. B* **2011**, *115* (12), 2717–2727. https://doi.org/10.1021/jp1112125.

(67) Newman, J.; Thomas-Alyea, K. E. *Electrochemical Systems*; John Wiley & Sons: New York, 2004.

(68) Weber, A. Z.; Delacourt, C. Mathematical Modelling of Cation Contamination in a Proton-Exchange Membrane. *Fuel Cells* **2008**, *8* (6), 459–465. https://doi.org/10.1002/fuce.200800044.

(69) Delacourt, C.; Newman, J. Mathematical Modeling of a Cation-Exchange Membrane Containing Two Cations. *J. Electrochem. Soc.* **2008**, *155* (11), 1210–1217. https://doi.org/10.1149/1.2977960.

(70) Banham, D.; Ye, S.; Cheng, T. T. H.; Knights, S.; Stewart, S. M.; Garzon, F. Impact of CeOx Additives on Cathode Catalyst Layer Poisoning. *ECS Trans.* **2013**, *58* (1), 369–380. https://doi.org/10.1149/05801.0369ecst.